Probing confinement resonances by photoionizing Xe inside a C_{60}^+ molecular cage

R. A. Phaneuf,[1,*] A. L. D. Kilcoyne,[2] N. B. Aryal,[1] K. K. Baral,[1] D. A. Esteves-Macaluso,[3] C. M. Thomas,[1] J. Hellhund,[1,4] R. Lomsadze,[1,5] T. W. Gorczyca,[6] C. P. Ballance,[7] S. T. Manson,[8] M. F. Hasoglu,[9] S. Schippers,[4] and A. Müller[4]

[1]*Department of Physics, University of Nevada, Reno, Nevada 89557-0220, USA*

[2]*Advanced Light Source, MS 7-100, Lawrence Berkeley National Laboratory, Berkeley, California 94720, USA*

[3]*Department of Physics and Astronomy, University of Montana, Missoula, Montana 59812, USA*

[4]*Institut für Atom- und Molekülphysik, Justus-Liebig-Universität Giessen, D-35392 Giessen, Germany*

[5]*Faculty of Exact and Natural Sciences, Tbilisi State University, Chavchavadze Av. 3, 0128 Tbilisi, Republic of Georgia*

[6]*Department of Physics, Western Michigan University, Kalamazoo, Michigan 49008-5252*

[7]*Department of Physics, Auburn University, Auburn, Alabama 36849, USA*

[8]*Department of Physics and Astronomy, Georgia State University, Atlanta, Georgia 30303-4106, USA*

[9]*Hasan Kalyoncu University, 27100 Sahinbey, Gaziantep, Turkey*

(Received 6 September 2013; published 1 November 2013)

Double photoionization accompanied by loss of n C atoms ($n = 0$, 2, 4, 6) was investigated by merging beams of $Xe@C_{60}^+$ ions and synchrotron radiation and measuring the yields of product ions. The giant 4*d* dipole resonance of the caged Xe atom has a prominent signature in the cross section for these product channels, which together account for 6.2 ± 1.4 of the total Xe 4*d* oscillator strength of 10. Compared to that for a free Xe atom, the oscillator strength is redistributed in photon energy due to multipath interference of outgoing Xe 4*d* photoelectron waves that may be transmitted or reflected by the spherical C_{60}^+ molecular cage, yielding so-called confinement resonances. The data are compared with an earlier measurement and with theoretical predictions for this single-molecule photoelectron interferometer system. Relativistic *R*-matrix calculations for the Xe atom in a spherical potential shell representing the fullerene cage show the sensitivity of the interference pattern to the molecular geometry.

DOI: 10.1103/PhysRevA.88.053402 PACS number(s): 32.80.Fb, 32.70.Cs, 32.80.Aa

I. INTRODUCTION

Shortly following the discovery of the C_{60} fullerene molecule by Kroto and collaborators [1], endofullerene molecules ($A@C_{60}$) were suggested that contain an atom A inside the spherical carbon cage [2]. The existence of such exotic molecules was initially controversial but was firmly established several years later in the same laboratory [3]. Numerous practical applications of endofullerene molecules were proposed and are being developed, among them in advanced computing [4], photovoltaics [5], hydrogen storage [6], and medicine [7]. Novel quantum effects associated with photoionizing an atom located within a spherical shell were predicted [8] and subsequently termed confinement resonances [9]. The phenomenon is caused by multipath quantum interference of photoelectron waves emitted by the encaged atom that may be transmitted or reflected by the carbon cage. The interference is manifested in the total photoionization cross section because of the direct correspondence between photon and photoelectron energies. The effect is expected to be particularly strong for a Xe atom encaged in C_{60}. Photoabsorption by a free xenon atom with a filled 4*d* subshell leads to a giant resonance in photoionization near 100 eV, as shown in Fig. 1, and Xe is expected to be centered within the C_{60} cage. Numerous theoretical calculations of the Xe 4*d* giant resonance in photoionization of $Xe@C_{60}$ using different approximations predict a redistribution of the oscillator strength as a function of photon energy compared to that for a free Xe atom. The interference is prominent because the de Broglie wavelengths of photoelectrons in the 70–140 eV photon energy range of the broad Xe 4*d* resonance are comparable to the ∼0.7 nm diameter of the C_{60} molecular cage. The calculations show that the predicted interference pattern is sensitive to the thickness of the cage and to the position of the atom within.

Because noble-gas endofullerenes were unavailable in sufficient quantity, the flourish of theoretical activity on the subject of confinement resonances continued for nearly two decades [8–16] in the absence of an experimental test, and even their existence was questioned [17]. The first experimental hint of this phenomenon was reported by Kilcoyne *et al.* [18] in the total cross section for double photoionization of $Xe@C_{60}^+$ accompanied by loss of two carbon atoms. The experiment was conducted at the Advanced Light Source (ALS) by merging a mass-selected ion beam with a beam of monochromatized synchrotron radiation. These initial measurements, shown in Fig. 1, are suggestive of the predicted interference phenomenon but because of extremely low product-ion count rates, their statistical precision was insufficient to distinguish among the theoretical predictions.

This proof-of-principle experimental demonstration with $Xe@C_{60}^+$ [18] motivated a concerted effort to increase ion beam current available for merged-beams measurements. A resulting factor of 40 increase in ion current made it possible to experimentally investigate confinement resonances in unprecedented detail. The results of these investigations and of new theoretical calculations are reported here. The comparison between experiment and theory reveals details of the confining fullerene potential.

*phaneuf@unr.edu

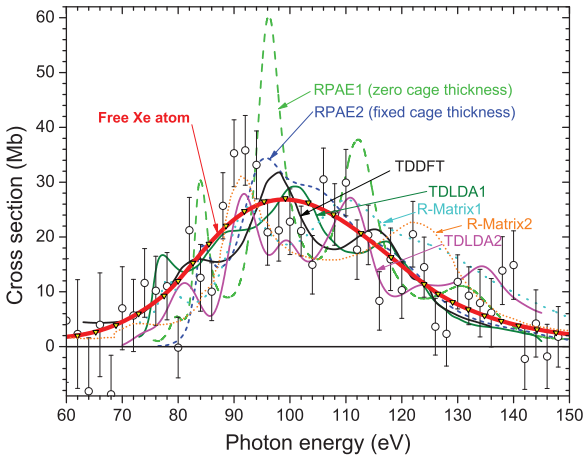

FIG. 1. (Color online) Theoretical calculations of the cross sections for photoionization of endohedral Xe@C_{60}, showing the predictions in different approximations for redistribution of Xe 4*d* oscillator strength due to confinement resonances. Time-dependent density functional theory (TDDFT) (solid black curve) [8], random phase approximation with exchange (RPAE1) (dashed green curve) [10], RPAE2 (dashed blue curve) [12], time-dependent local density approximation (TDLDA1) (solid green curve) [13], TDLDA2 (solid magenta curve) [14], *R*-matrix1 (dotted cyan curve) [15] and *R*-matrix2 (dotted orange curve) [16]. The experimental results [18] for Xe@C_{60}^+ are shown as circles with error bars. The data have been scaled in cross section to give an integral oscillator strength of 10 in this energy region, corresponding to a filled Xe 4*d* subshell. For comparison, the photoionization cross section for the free Xe atom is shown as a thick solid red curve, as recommended by West and Morton [19].

II. METHODS

A. Experiment

Since Xe@C_{60} is commercially unavailable, a setup was developed at the ALS based on an ion implantation technique to produce endofullerenes introduced by Tellgmann *et al.* [20] for alkali atoms and by Shimshi *et al.* [21] for He atoms to produce endohedral samples for later evaporation into an ion source [18]. During a period of several months prior to the photoionization measurements, a 100–200 eV beam of Xe^+ ions with a current of several μA from an ion sputter gun bombarded the surface of a rotating stainless steel cylinder onto which sublimed C_{60} powder of 99.95% purity was being continuously deposited in vacuum by evaporation. The powder deposited on the cylinder (several hundred mg) was then scraped from the surface and placed into a small oven for subsequent reevaporation into a low-power Ar discharge in an electron-cyclotron-resonance (ECR) ion source [22]. A very small fraction ($\sim 10^{-5}$) of the C_{60} molecules in the accumulated samples contained a Xe atom. These samples yielded pure mass per charge-analyzed beams of Xe@C_{60}^+ ions with a current in the range of 0.1–0.3 pA. While such small ion beam currents were sufficient for the proof-of-principle measurement reported by Kilcoyne *et al.* [18] (Fig. 1), it was evident that a definitive result would require substantially increased ion beam current.

To this end, a strategy was devised to use isotopically enriched ^{136}Xe rather than natural Xe in the synthesis, since at low mass resolution the nine stable isotopes (none dominant) yielded a broad Xe@C_{60}^+ mass peak with low intensity. Using ^{136}Xe provided a twofold advantage. First, the ^{136}Xe@C_{60}^+ peak in the ion mass spectrum became narrower, increasing the ion beam current. Second, the ^{136}Xe@C_{60}^+ mass peak was further removed from that of C_{70}^+, the major contaminant in the 99.95% pure C_{60} material used in the synthesis. This provided complete separation of the ^{136}Xe@C_{60}^+ ion mass peak from that of C_{70}^+ at much lower mass resolution, allowing the ion beam defining slits to be opened wider, and further increasing the ion beam current available for a photoionization measurement. Other improvements in the sample yield resulted from a systematic optimization of the parameters for the synthesis: Xe^+ ion beam energy ($\sim$130 eV), rotation speed of the metal cylinder ($\sim$1 Hz), and C_{60} evaporation rate ($\sim$1 mg/hr). The effective Xe@C_{60} yield in the prepared samples was increased from 1×10^{-5} to 2×10^{-4}, and the peak ion beam current available for a merged-beams measurement from 0.14 pA to 5.6 pA. Ion beam mass spectra measured at both high and low mass resolution illustrating this improvement are presented in Fig. 2. The isotope-resolved high-resolution spectra were measured with narrow ion-beam defining slits using a single-particle detector, whereas the low-resolution spectra correspond to the conditions for merged-beams measurements. As shown in the right two panels, this resulted in a comparable mass separation of C_{70}^+ and Xe@C_{60}^+, but with the ^{136}Xe@C_{60}^+ ion beam current approximately 40 times greater.

The photoionization measurements were performed using the ion photon beam (IPB) end station on the ALS undulator beamline 10.0.1 [23,24]. A collimated and mass-selected beam of ^{136}Xe@C_{60}^+ ions was electrostatically guided onto the axis of a counterpropagating beam of monochromatized synchrotron radiation. The two beams were merged along a common path of approximately 1.4 m. The ion beam was subsequently demerged from the photon beam by a dipole magnet that also separated further ionized product ions from the primary ion beam and directed them to a single-particle detector with a dark count rate of 0.02 Hz [25]. The primary ion beam was collected in a Faraday cup and its current measured with fA resolution. The photon beam was directed onto a calibrated Si x-ray photodiode, which provided a measure of its intensity. For absolute measurements the spatial overlap of the beams in a central electrostatically biased interaction region of length 29.4 ± 0.6 cm was quantified using three translating-slit scanners located near the beginning, middle and end of their common interaction path.

Cross-section scans were carried out by merging the ion and photon beams and stepping the photon energy over the range 60–150 eV in 0.5 eV increments. Product ions were counted for typically 10 s at each photon energy and the scan was repeated until the standard deviation due to the random uncertainty at each energy was typically 5% or less. Signal count rates ranged from 0.5–15 Hz, dependent on the primary ion beam current, the selected product ion, and the photon energy.

The relatively low primary ion beam currents of Xe@C_{60}^+ and limitations on photon beamtime at the ALS made independent absolute cross-section measurements impractical. To place the measurements with Xe@C_{60}^+ on an absolute scale,

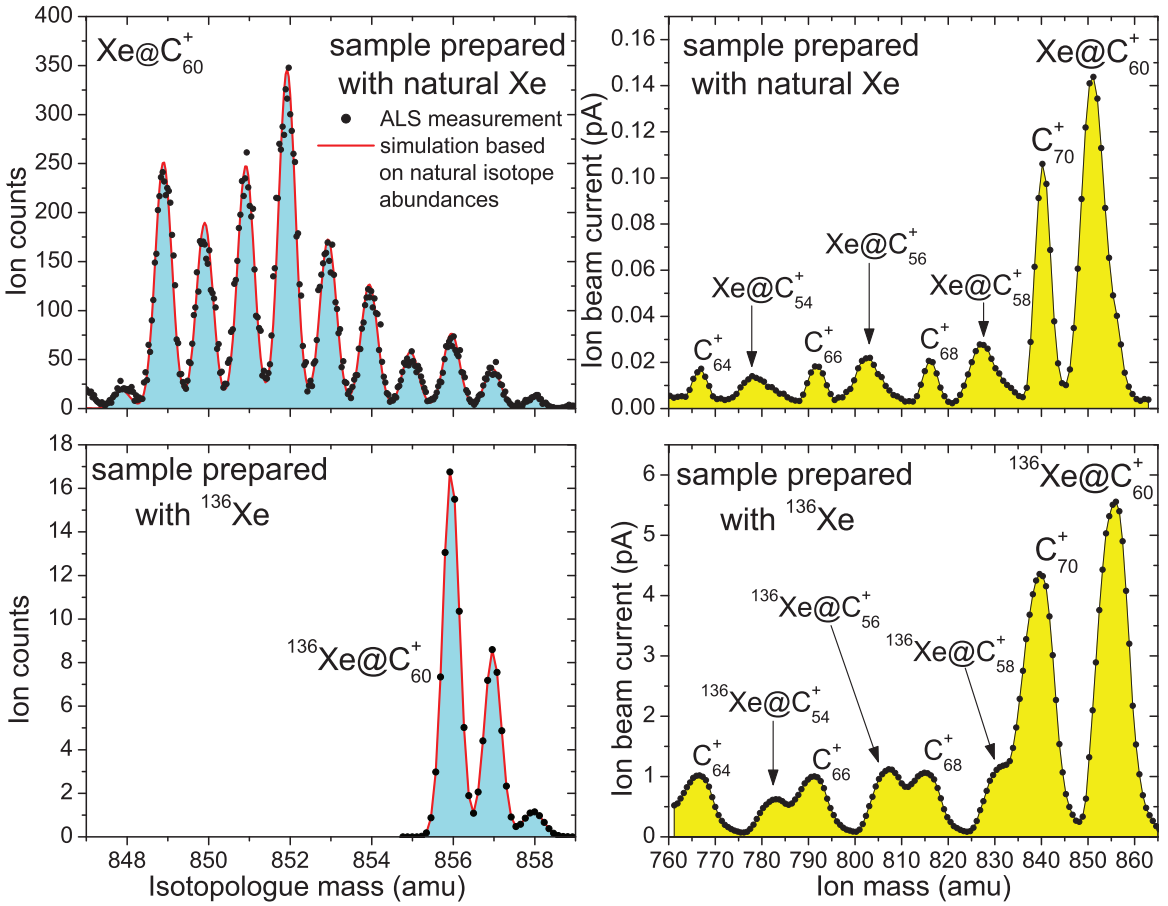

FIG. 2. (Color online) Ion beam mass spectra measured at high mass resolution (left panels), and low mass resolution (right panels). Upper panels are for samples prepared with a natural mixture of Xe isotopes, and lower panels for samples prepared with highly enriched ^{136}Xe. The three peaks in the lower left spectrum correspond to $^{136}Xe@C_{60}^{+}$ containing zero, one and two ^{13}C atoms. The top right panel corresponds to the conditions for the merged-beams experiment of Kilcoyne *et al.* [18] and the lower right for the current measurements.

corresponding empty-cage cross sections were measured with C_{60}^{+}, to which the relative cross sections for the endohedral ion were normalized at photon energies in the ranges 60–65 eV and 145–150 eV. In these photon energy ranges, negligible contributions to the cross section from the caged Xe atom were expected.

B. Theory

Realistic theoretical treatment of $Xe@C_{60}$ confinement resonances requires precise modeling of the atomic photoionization and of the subsequent interaction of the outgoing, predominantly f-wave photoelectron with the confining fullerene. As indicated by the comparison in Fig. 1, there are considerable differences between the various theoretical cross sections shown. This is partly due to the different levels of sophistication in treating the atomic Xe photoionization. The corresponding cross sections differ because the energy of the $4d^{-1}$ threshold, and the relative position of the strong $4d \rightarrow \epsilon f$ shape resonance relative to threshold, vary depending on the degree of electron correlation included in each theoretical calculation. Furthermore, the additional oscillatory signal in the total $Xe@C_{60}$ cross section is highly dependent on the theoretical modeling of the fullerene potential. For instance, the physically unrealistic δ-function model used in one of the random-phase calculations (RPAE1 in Fig. 1) produces oscillations that are clearly too large in amplitude and even the different inner and outer radii of the model square-well potentials that are used for the TDLDA and TDDFT or R-matrix calculations give different oscillatory wavelengths. Thus in the present work the atomic photoionization is first described as accurately as possible by benchmarking to the experimental Xe photoionization cross section. This guarantees the correct underlying atomic subshell cross section. Then, in the second step, an optimal square-well potential is used to reproduce the confinement-induced oscillations observed in the present $Xe@C_{60}^{+}$ experiment.

In order to describe the free Xe photoionization accurately, the relativistic Dirac atomic R-matrix code (DARC) [26,27] was utilized to improve upon earlier nonrelativistic R-matrix calculations [15]. As in the earlier study, all channels associated with single-electron promotions were included, giving rise to a five-level description of the Xe^{+} photoion—$4d^{10}5s^{2}5p^{5}(^{2}P_{3/2,1/2})$, $4d^{10}5s5p^{6}(^{2}S_{1/2})$, and $4d^{9}5s^{2}5p^{6}(^{2}D_{5/2,3/2})$. However, this also permitted the all-important $4d^{2}$–$4f^{2}$ two-electron correlation to be included, not only in the neutral Xe $4d^{10}5s^{2}5p^{6}(^{1}S_{0})$ initial state, as was done earlier, but also in the final, strong $4d^{9}5s^{2}5p^{6}\epsilon f$ channels. The latter correlation could not be included in

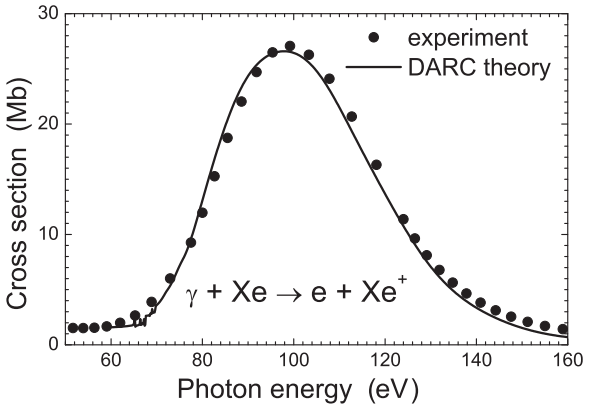

FIG. 3. Comparison of present DARC R-matrix calculation with recommended experimental data for photoionization of a free Xe atom [19].

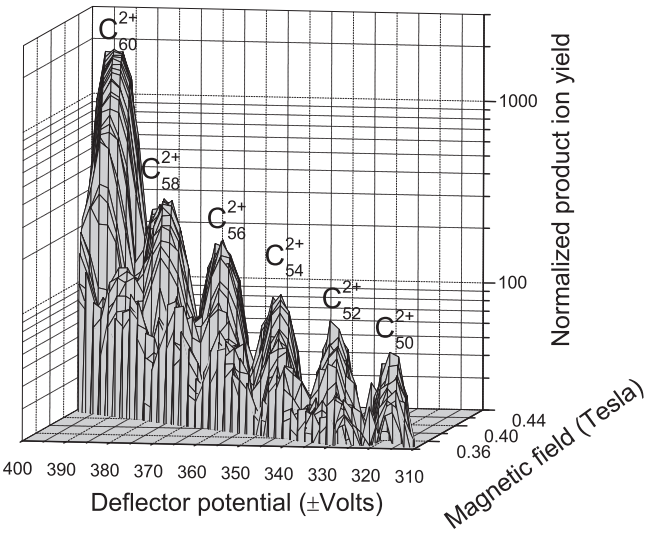

FIG. 4. Two-dimensional doubly charged product ion scans for a primary ion beam of C_{60}^{+} measured at a fixed photon energy of 65 eV. The demerging magnet and spherical electrostatic plates deflect the product ions across the detector in orthogonal directions [23], permitting scans of the photo-product space.

the nonrelativistic codes [28,29] due to their restriction to maximum double f-subshell occupancy. The resulting cross section for Xe now shows that the shape and strength of the giant $4d \rightarrow \epsilon f$ resonance is in excellent agreement with the recommended experimental data for a free Xe atom [19], as illustrated in Fig. 3.

Given an accurate R-matrix cross section for free Xe photoionization, the dimensions for the additional, model spherical-well cage potential,

$$V_c(r) = \begin{cases} -U_0, & r_0 \leqslant r \leqslant r_1 \\ 0, & \text{otherwise} \end{cases}, \qquad (1)$$

which best reproduce the confinement resonances observed in the experiment could also be included, thereby allowing additional information on the fullerene potential to be extracted. Lastly, in order to compare to the experimental results, it was also necessary to consider the charge of the $Xe@C_{60}^{+}$ confining cage. The only additional effect this has is to suppress photoionization into newly opened channels until an additional $e^2/(4\pi\epsilon_0 r_1)$ (=3.73 eV for $r_1 = 0.33$ nm) in photon energy is reached. This is to account for the additional Coulomb potential of the charged $Xe@C_{60}^{+}$ ion that the escaping photoelectron must overcome, and gives rise to a delayed ionization threshold (71.28 eV for $r_1 = 0.33$ nm). Both the free Xe and caged $Xe@C_{60}^{+}$ R-matrix cross sections have been shifted in photon energy so that the theoretical $4d^9 5s^2 5p^6(^2D_{5/2})$ photoelectron threshold energy of the free Xe atom is aligned with the experimental value of 67.55 eV [32].

III. RESULTS AND DISCUSSION

Photoionization of the Xe $4d$ subshell creates an inner vacancy that decays predominantly by Auger electron emission, resulting in net double ionization. As expected, measurements of single photoionization of $Xe@C_{60}^{+}$ yielding $Xe@C_{60}^{2+}$ products in the 60–150 eV photon energy range showed no evidence for the presence of Xe. The measured photon energy dependences of the $Xe@C_{60}^{2+}$ photoion yield from $Xe@C_{60}^{+}$ were identical, within experimental uncertainties, to those measured for C_{60}^{2+} products from C_{60}^{+}.

Preliminary measurements with C_{60}^{+} ions in this photon energy range indicated that photoionization accompanied by loss of one or more pairs of C atoms has significant probability, as shown in Fig. 4.

Therefore, with a primary ion beam of endohedral $Xe@C_{60}^{+}$, the product ions $Xe@C_{60-n}^{3+}$ ($n = 0, 2, 4, 6$) were considered to be optimal candidates for observation of Xe $4d$ photoionization signatures. The measured cross sections for these products are presented in Fig. 5 along with the corresponding empty-cage measurements (Table I) to which they are normalized. The data were taken with a photon energy resolution that decreased smoothly from 0.1 eV at 60 eV to 0.2 eV at 150 eV. $^{136}Xe@C_{60}^{+}$ ion beam currents ranged from 1.5 pA to 5.6 pA, resulting in significantly improved statistical precision and smaller error bars compared to the earlier results reported by Kilcoyne *et al.* [18] for the $Xe@C_{58}^{3+}$ product channel. The present data were also taken with 0.5 eV photon energy steps, compared to 2 eV steps for the previous measurements. Strong enhancement of the cross sections due to $4d$ photoionization of the encaged Xe atom is found in this energy range beginning at the onset of ionization of the Xe $4d$ subshell. A feature near 75 eV is evident that was not identifiable in the data of Kilcoyne *et al.* [18] because of the coarser energy grid and much larger statistical uncertainty. The net Xe $4d$ contributions to the cross sections were estimated by subtracting the empty-cage cross sections measured with C_{60}^{+} from the corresponding measurements with $^{136}Xe@C_{60}^{+}$. The resulting individual Xe $4d$ contributions for the different products are presented in Fig. 6 and compared with their sum. The photon energy dependences for each product channel are similar. A somewhat surprising result is that the $^{136}Xe@C_{56}^{3+}$ product channel has the strongest Xe $4d$ photoionization signature among those investigated. The corresponding Xe $4d$ oscillator strengths do not decrease monotonically with the number of C atoms lost as do the cross sections for single ionization of C_{60}^{+} accompanied by loss of pairs of C atoms (Fig. 4 and Table I). Together, these products account for 6.2 ± 1.4 of the total Xe $4d$ oscillator strength of 10. Evidently additional products may be created

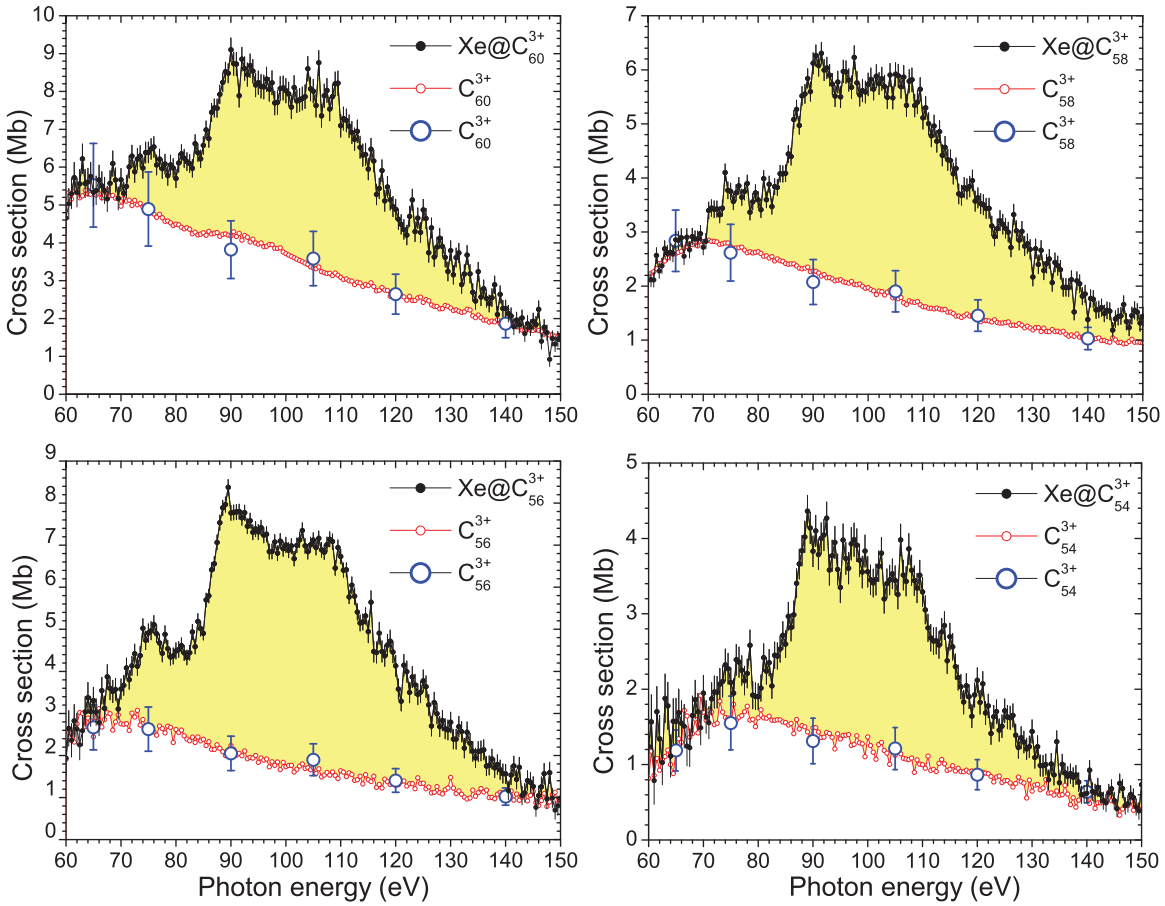

FIG. 5. (Color online) Measured cross sections for double photoionization of $^{136}Xe@C_{60}^{+}$ accompanied by the loss of 0, 2, 4, and 6 C atoms (solid circles) along with their corresponding empty-cage cross sections (open circles). Blue circles with error bars denote absolute measurements from Table I. Strong enhancement due to Xe 4*d* photoionization is evident.

with appreciable probability subsequent to Xe 4*d* ionization. Indeed, preliminary measurements of $Xe@C_{58}^{4+}$ product ions also show evidence of the Xe 4*d* feature and will be the subject of future experiments.

The sum of the Xe 4*d* contributions for the different product ions investigated (Fig. 6) is compared in Fig. 7 with the present Dirac *R*-matrix theoretical calculations. Figure 8 presents a comparison of the experimental result with the nonrelativistic [15] and relativistic *R*-matrix calculations (current Rmat2 and Ref. [16]). For a yet more sensitive test of the theoretical results and for illustrating the effect

TABLE I. Measured absolute cross sections for single photoionization of C_{60}^{+} and relative cross sections for C_{60}^{+} yielding C_{60-n}^{2+} (n = 2, 4, 6) and C_{60-n}^{3+} products (n = 0, 2, 4, 6) determined from measured signal ratios under identical conditions. Absolute uncertainties in the tabulated values are estimated to be ±22%.

Photon Energy (eV)	Products C_{60}^{2+} (Mb)	– C_{58}^{2+} (Mb)	– C_{56}^{2+} (Mb)	– C_{54}^{2+} (Mb)	– C_{60}^{3+} (Mb)	– C_{58}^{3+} (Mb)	– C_{56}^{3+} (Mb)	– C_{54}^{3+} (Mb)
65	57.5	13.0	11.1	6.5	5.5	2.8	2.7	1.2
75	43.8	9.9	8.0	4.2	4.9	2.6	2.6	1.6
90	28.4	6.0	4.8	2.4	3.8	2.1	2.1	1.3
105	22.4	4.8	3.7	1.8	3.6	1.9	1.9	1.2
120	17.3	3.8	2.8	1.4	2.6	1.5	1.4	0.9
140	13.2	3.0	2.2	1.0	1.9	1.0	1.0	0.6

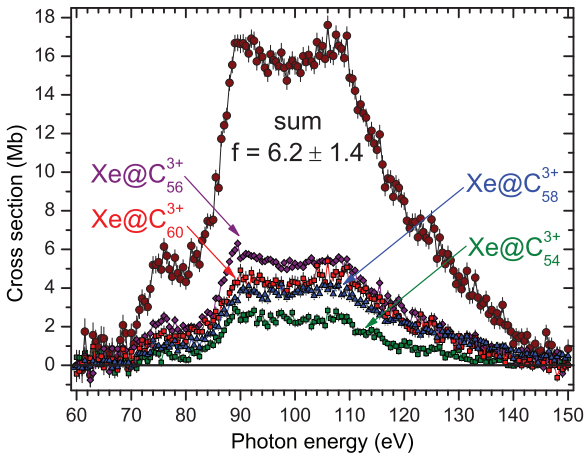

FIG. 6. (Color online) Net Xe 4*d* contributions to double photoionization of $^{136}Xe@C_{60}^{+}$ accompanied by the loss of n = 0, 2, 4 and 6 C atoms, along with their sum. The individual oscillator strengths found in the different channels are 1.71 ± 0.38 (n = 0), 1.51 ± 0.33 (n = 2), 2.10 ± 0.46 (n = 4), and 0.85 ± 0.19 (n = 6).

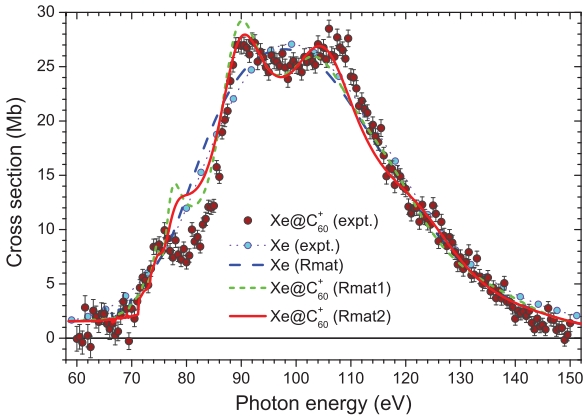

FIG. 7. (Color online) Comparison of the present measurements for the sum of Xe 4*d* contributions from Fig. 6 with the present *R*-matrix results for photoionization of Xe@C_{60}^+. Two sets of parameters for the shell potential were applied: $r_0 = 0.31$ nm, $r_1 = 0.40$ nm, $U_0 = 8.8$ V (Rmat1, green short-dashed curve) and $r_0 = 0.33$ nm, $r_1 = 0.39$ nm, $U_0 = 8.2$ V (Rmat2, red solid curve). The experimental results have been scaled to give an integral oscillator strength of 10 in this energy range. Also shown are the experimental data [19] (blue open circles) and the present *R*-matrix results (blue long-dashed curve) for photoionization of the free Xe atom.

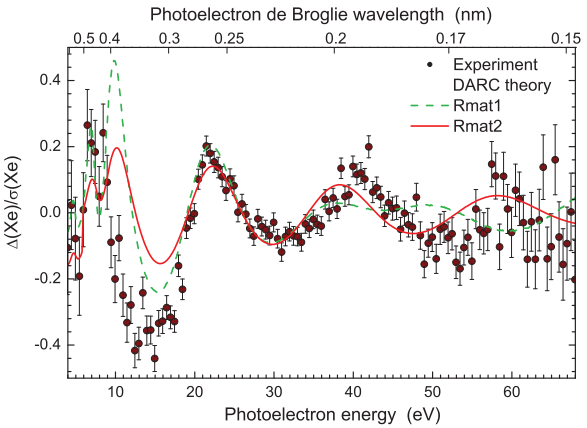

FIG. 9. (Color online) Oscillatory structure of the encapsulated-Xe photoionization cross section made visible by displaying the ratio $\Delta(\mathrm{Xe})/\sigma(\mathrm{Xe}) = [\sigma(\mathrm{Xe@C_{60}^+})\text{-}\sigma(\mathrm{Xe})]/\sigma(\mathrm{Xe})$ as a function of the photoelectron energy and the photoelectron de Broglie wavelength, respectively. The experimental and theoretical data result from the cross sections provided in Fig. 7. For determining the experimental data points the $\sigma(\mathrm{Xe})$ data of West and Morton [19] were combined with the present results for the sum of all Xe 4*d* contributions to $\sigma(\mathrm{Xe@C_{60}^+})$. At a 4*d* photoelectron energy of 21 eV, about five de Broglie half waves fit inside the inner diameter of the C_{60} cage.

of quantum interference inside a molecular sphere Fig. 9 shows $\Delta(\mathrm{Xe})/\sigma(\mathrm{Xe}) = [\sigma(\mathrm{Xe@C_{60}^+})\text{-}\sigma(\mathrm{Xe})]/\sigma(\mathrm{Xe})$, i.e., the relative deviation of the Xe 4*d* photoabsorption cross section of the encapsulated versus that of the free Xe atom. By sampling a wide range of values for the inner and outer radii, r_0 and r_1, and well depth U_0, it was determined that no single set of dimensions, and therefore no single spherical well, was adequate for modeling all of the experimentally observed oscillations. For instance, using a relatively small inner radius, such as $r_0 \approx 0.16$ nm, along with an outer radius of $r_1 \approx 0.37$ nm, the oscillatory structure seen at lower photon energies (≈70–85 eV) in the experiment could be reproduced, whereas a larger inner radius of $r_0 \approx 0.33$ nm was necessary

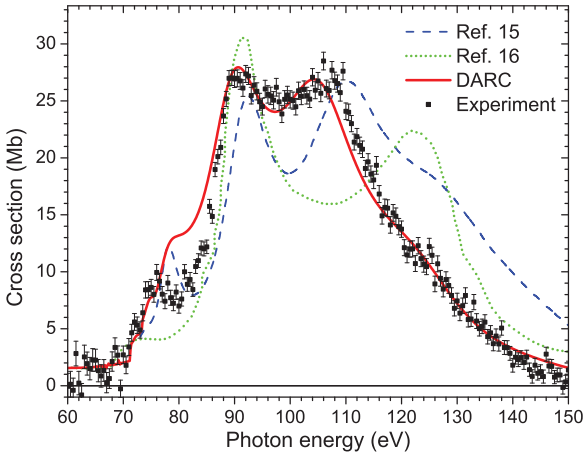

FIG. 8. (Color online) Comparison of the present measurements for the sum of Xe 4*d* contributions from Fig. 6 with nonrelativistic *R*-matrix calculation [15] (dashed blue curve) and relativistic *R*-matrix calculations (Ref. [16], dotted green curve and current DARC Rmat2 calculation, solid red curve) for photoionization of Xe@C_{60}^+.

to adequately describe the oscillations seen near the peak of the cross section and at higher photon energies. Therefore those latter dimensions ($r_0 = 0.33$ nm, $r_1 = 0.39$ nm, and $U_0 = 8.2$ V) were chosen to model the higher confinement resonances adequately. Although it produces a slightly larger sum of squared deviations from the measured cross sections, a different set of parameters ($r_0 = 0.31$ nm, $r_1 = 0.40$ nm, and $U_0 = 8.8$ V) is also considered because it demonstrates the possibility for reproducing the experimentally observed peak feature between 70 eV and 80 eV. This parameter set implies a radius 0.35 nm of the C_{60} skeleton close to what has been found in the past [30,31]. However, the present findings indicate a thickness of the carbon shell $\delta = r_1 - r_0$ considerably smaller than the previously determined value of 0.15 nm [31].

Note that the inability to model all of the oscillatory features quantitatively emphasizes the limitation of the single spherical-well approximation employed. Although the major backscattering of the ejected photoelectron wave undoubtedly occurs at the inner and outer radii of the fullerene shell, the approximation that the potential in the interior of the shell is constant, engendering no additional scattering, is certainly too severe. The best-fit shell parameters obtained with this simple potential may therefore be somewhat unphysical, and further *R*-matrix calculations with a physically more realistic potential would be illuminating.

IV. SUMMARY AND CONCLUSIONS

Clear experimental evidence is presented for redistribution of the oscillator strength associated with Xe 4*d* photoionization in the endohedral molecular ion Xe@C_{60}^+. This phenomenon is caused by multipath quantum interference of photoelectron waves that may be transmitted or reflected by the spherical fullerene shell in this highly symmetric endohedral molecule. Xe@C_{60}^{3+}, Xe@C_{58}^{3+}, Xe@C_{56}^{3+}, and

$Xe@C_{54}^{3+}$ products together account for more than 60% of the total Xe $4d$ oscillator strength. Comparison of the measurements with the results of new Dirac R-matrix theoretical calculations for $Xe@C_{60}$ illustrates the sensitivity of the interference structure to the molecular geometry. The level of agreement between theory and experiment validates the use of a potential as a quantitative description of the C_{60} cage in an energy region far from the C_{60} plasmons, and demonstrates that the many-electron, multichannel, open-shell capabilities of the R-matrix method may be applied to the photoionization of confined-atom systems in general.

The caged Xe atom serves as an internal electron source in this single-molecule interferometer, probing details of the electronic structure of the encaging molecule from within. A remarkable finding is that $4d$ photoionization of the encaged Xe atom leads to enhanced fragmentation of the C_{60} cage, as evidenced by the yields of the C_{60-n}^{3+} photoproducts with $n = 2,4,6$. The caged Xe atom is obviously an efficient converter of photon energy to molecular vibrational energy. This may be useful for cancer therapy or for nanostructuring of solid surfaces, where damage to a molecular or crystalline environment must be applied in a controlled and well localized manner.

The present experiment pushed the sensitivity of the photon-ion merged beam technique to new limits. Quantitative results with low statistical uncertainty were obtained from minute amounts of probe material that would be far too little for a conventional gas-phase photoabsorption experiment with neutral molecular vapor.

ACKNOWLEDGMENTS

This research was supported by the Chemical Sciences, Geosciences and Biosciences Division, Office of Basic Energy Sciences, Office of Science, US Department of Energy under Grant No. DE-FG02-03ER15424. Additional funding was provided by the Office of Basic Energy Sciences, US Department of Energy under Contract No. DE-AC03-76SF0098 and by the Deutsche Forschungsgemeinschaft.

[1] H. W. Kroto, J. R. Heath, S. C. O'Brien, R. F. Curl, and R. E. Smalley, Nature (London) **318**, 162 (1985).
[2] J. R. Heath, S. C. O'Brien, Q. Zhang, Y. Liu, R. F. Curl, F. K. Tittel, and R. E. Smalley, J. Am. Chem. Soc. **107**, 7779 (1985).
[3] Y. Chai, T. Guo, C. Jin, R. E. Haufler, L. P. F. Chibante, J. Fure, L. Wang, J. M. Alford, and R. E. Smalley, J. Phys. Chem. **95**, 7564 (1991).
[4] W. Harneit, Phys. Rev. A **65**, 032322 (2002).
[5] R. B. Ross, C. M. Cardona, D. M. Guldi, S. G. Sankaranarayanan, M. O. Reese, N. Kopidakis, J. Peet, B. Walker, G. C. Bazan, E. V. Keuren, B. C. Holloway, and M. Drees, Nature Mater. **8**, 208 (2009).
[6] O. V. Pupysheva, A. A. Farajian, and B. I. Yakobson, Nano Letters **8**, 767 (2008).
[7] K. B. Hartman, L. J. Wilson, and M. G. Rosenblum, Mol. Diag. Ther. **12**, 1 (2008).
[8] M. J. Puska and R. M. Nieminen, Phys. Rev. A **47**, 1181 (1993).
[9] J. P. Connerade, V. K. Dolmatov, and S. T. Manson, J. Phys. B: At. Mol. Opt. Phys. **33**, 2279 (2000).
[10] M. Ya. Amusia, A. S. Baltenkov, L. V. Chernysheva, Z. Felfli, and A. Z. Msezane, J. Phys. B: At. Mol. Opt. Phys. **38**, L169 (2005).
[11] M. Ya. Amusia, A. S. Baltenkov, and L. Chernysheva, JETP Letters **87**, 200 (2008).
[12] V. K. Dolmatov and S. T. Manson, J. Phys. B: At. Mol. Opt. Phys. **41**, 165001 (2008).
[13] M. E. Madjet, T. Renger, D. E. Hopper, M. A. McCune, H. S. Chakraborty, J.-M. Rost, and S. T. Manson, Phys. Rev. A **81**, 013202 (2010).
[14] Z. Chen and A. Msezane, Eur. Phys. J. D **66**, 184 (2012).
[15] T. W. Gorczyca, M. F. Hasoglu, and S. T. Manson, Phys. Rev. A **86**, 033204 (2012).
[16] B. Li, G. O'Sullivan, and C. Dong, J. Phys. B: At. Mol. Opt. Phys. **46**, 155203 (2013).
[17] A. V. Korol and A. V. Solov'yov, J. Phys. B: At. Mol. Opt. Phys. **43**, 201004 (2010).
[18] A. L. D. Kilcoyne, A. Aguilar, A. Müller, S. Schippers, C. Cisneros, G. Alna'Washi, N. B. Aryal, K. K. Baral, D. A. Esteves, C. M. Thomas, and R. A. Phaneuf, Phys. Rev. Lett. **105**, 213001 (2010).
[19] J. B. West and J. Morton, At. Data Nucl. Data Tables **22**, 103 (1978).
[20] R. Tellgmann, N. Krawez, S.-H. Lin, I. V. Hertel, and E. E. B. Campbell, Nature (London) **382**, 407 (1996).
[21] R. Shimshi, R. J. Cross, and M. Saunders, J. Am. Chem. Soc. **119**, 1163 (1997).
[22] F. Brötz, R. Trassl, R. W. McCullough, W. Arnold, and E. Salzborn, Phys. Scr. **T92**, 278 (2001).
[23] A. M. Covington, A. Aguilar, I. R. Covington, M. F. Gharaibeh, G. Hinojosa, C. A. Shirley, R. A. Phaneuf, I. Álvarez, C. Cisneros, I. Dominguez-Lopez, M. M. Sant'Anna, A. S. Schlachter, B. M. McLaughlin, and A. Dalgarno, Phys. Rev. A **66**, 062710 (2002).
[24] G. A. Alna'washi, M. Lu, M. Habibi, R. A. Phaneuf, A. L. D. Kilcoyne, A. S. Schlachter, C. Cisneros, and B. M. McLaughlin, Phys. Rev. A **81**, 053416 (2010).
[25] K. Rinn, A. Müller, H. Eichenauer, and E. Salzborn, Rev. Sci. Instrum. **53**, 829 (1982).
[26] P. H. Norrington and I. P. Grant, J. Phys. B: At. Mol. Opt. Phys. **20**, 4869 (1987).
[27] C. P. Ballance and D. C. Griffin, J. Phys. B: At. Mol. Opt. Phys. **39**, 3617 (2006).
[28] P. G. Burke, *R-matrix Theory of Atomic Collisions* (Springer, New York, 2011).
[29] K. A. Berrington, W. Eissner, and P. Norrington, Comput. Phys. Commun. **92**, 290 (1995).
[30] Y. B. Xu, M. Q. Tan, and U. Becker, Phys. Rev. Lett. **76**, 3538 (1996).
[31] A. Rüdel, R. Hentges, U. Becker, H. S. Chakraborty, M. E. Madjet, and J. M. Rost, Phys. Rev. Lett. **89**, 125503 (2002).
[32] G. C. King, M. Tronc, F. H. Read, and R. C. Bradford, J. Phys. B **10**, 2479 (1977).